RSC Advances

PAPER

View Article Online
View Journal | View Issue

Cite this: *RSC Adv.*, 2023, **13**, 33541

Visible light photoreforming of greenhouse gases by nano Cu–Al LDH intercalated with urea-derived anions†

Ayat A.-E. Sakr, *[a] Dalia R. Abd El-Hafiz,[b] Osama Elgabry,[a] Eman S. Abdullah,[a] Mohamed A. Ebiad[a] and Tamer Zaki[b]

The accumulation of anthropogenic greenhouse gases (GHGs) in the atmosphere causes global warming. Global efforts are carried out to prevent temperature overshooting and limit the increase in the Earth's surface temperature to 1.5 °C. Carbon dioxide and methane are the largest contributors to global warming. We have synthesized copper–aluminium layered double hydroxide (Cu–Al LDH) catalysts by urea hydrolysis under microwave (MW) irradiation. The effect of MW power, urea concentration, and M^{II}/M^{III} ratios was studied. The physicochemical properties of the prepared LDH catalysts were characterized by several analysis techniques. The results confirmed the formation of the layered structure with the intercalation of urea-derived anions. The urea-derived anions enhanced the optical and photocatalytic properties of the nano Cu–Al LDH in the visible-light region. The photocatalytic activity of the prepared Cu–Al LDH catalysts was tested for greenhouse gas conversion (CH_4, CO_2, and H_2O) under visible light. The dynamic gas mixture flow can pass through the reactor at room temperature under atmospheric pressure. The results show a high conversion percentage for both CO_2 and CH_4. The highest converted amounts were 7.48 and 1.02 mmol mL^{-1} g^{-1} for CH_4 and CO_2, respectively, under the reaction conditions. The main product was formaldehyde with high selectivity (>99%). The results also show the stability of the catalysts over several cycles. The current work represents a green chemistry approach for efficient photocatalyst synthesis, visible light utilization, and GHGs' conversion into a valuable product.

Received 11th September 2023
Accepted 9th November 2023

DOI: 10.1039/d3ra06190f

rsc.li/rsc-advances

1 Introduction

The greenhouse gases (GHGs) are those that absorb infrared radiation from the atmosphere, consequently trapping the heat energy that is emitted from the Earth's surface and causing global warming.[1] This action results in climate change, that causes irreversible losses and damage to the environmental and human systems.[2] Carbon dioxide (CO_2) is the largest contributor to global warming. According to the Kyoto Protocol, methane is considered a GHG.[3] It is a short-lived greenhouse gas compared with CO_2.[4] It is a potent greenhouse gas. The anthropogenic accumulation of GHGs in the atmosphere leads to the global warming phenomenon, where the temperature of the Earth's surface is higher than that before the industrial era by ~1.5 °C. To prevent temperature overshooting and to limit global warming to 1.5 °C, global efforts are carried out in order to get the CO_2 net zero emission scenario (NZE), where CO_2 emissions decline to zero by 2050.[5–7] The Global Methane Pledge is targeted to reduce about 30% of anthropogenic methane emissions by 2030.[8,9] This could be done by using a clean energy source and supporting the transition to a low-carbon energy system.[7] Reduction of the accumulation of GHGs in the atmosphere could be performed through their capture and utilization.[6,10] Utilizing GHGs to produce fuel is considered a sustainable fuel production pathway.[11] The main challenge is to overcome the stability and inertness of both CO_2 and CH_4 and activate them.[12–14]

Photoreforming is a process where valuable products can be produced through the redox reaction of an illuminated photocatalyst. Thus, it utilizes light energy (solar) to produce fuel or chemical feedstock.[15] This process is considered an eco-friendly conversion process.[16] Photocatalytic partial oxidation of methane could be done using CO_2 and/or H_2O as soft oxidants. This process produces C1 platform molecules (such as formaldehyde, methanol, and carbon monoxide). Furthermore, higher hydrocarbons than methane (C2+) could be produced and are considered value-added products.[10,12]

Layered double hydroxide (LDH) or hydrotalcite-like materials are two-dimensional and classified as anionic clays. It is composed of positively charged (brucite-like) layers, with its

[a]*Gas Chromatogarphy Lab, Analysis & Evaluation Division, Egyptian Petroleum Research Institute, Nasr City, Cairo 11727, Egypt. E-mail: ayatsakr@yahoo.com; ayatsakr78@gmail.com; ayatsakr@epri.sci.eg*

[b]*Catalysis Lab, Petroleum Refining Division, Egyptian Petroleum Research Institute, Nasr City, P.B. 11727, Cairo, Egypt*

† Electronic supplementary information (ESI) available. See DOI: https://doi.org/10.1039/d3ra06190f

anion counterpart located in the interlayer space. The layers consist of metal cations that are octahedrally surrounded by six hydroxide ions. The octahedral units form infinite two-dimensional layers by edge-sharing. A three-dimensional structure is formed by the stacking of the layers on top of each other. The positive charge nature of the layer arises from replacing the M^{2+} cation with the M^{3+} cation.[17,18] The LDH general formula is $[M_{1-x}^{2+}M_x^{3+}(OH)_2]^{x+}(A_{x/n}^{n-})\cdot mH_2O$ where ($M^{2+} = Mg^{2+}$, Ca^{2+}, Zn^{2+},…); ($M^{3+} = Al^{3+}$, Cr^{3+}, Co^{3+},…), and x is the molar ratio of $M^{3+}/(M^{2+} + M^{3+})$; $0.2 \leq x \leq 0.33$.[19] The counterpart interlayer anion (A^{n-}) could be inorganic (*e.g.*, halides, nitrate, and carbonate) or organic (*e.g.*, polymers, anionic drugs, and amino acids).[17,18,20] The LDH materials have many potential applications in many fields, such as catalysis, adsorption, the chemical industry, and medical applications.[20] Recently, LDH materials have been applied in energy conversion and storage[21] and renewable energy production.[22] It can be functionalized to be used as a sensor and light-emitting material.[23] LDH materials are used as photocatalysts for CO_2 or methane conversion.[22,24–26]

Due to the structural features of the LDH, which permit the good distribution of the metals within the layer structure, and due to the good catalytic properties of copper,[27] we aimed to prepare LDH materials containing copper and aluminium (Cu–Al LDH) to be used as a photocatalyst for GHGs conversion. The Cu–Al LDH materials are precipitated homogeneously by the urea hydrolysis process. Urea is considered a precipitating agent because, when hydrolyzed, it produces hydroxide ions that raise the pH of the solution, consequently resulting in metal hydroxide precipitation. Its hydrolysis rate depends mainly on the temperature.[20] We have used microwave (MW) irradiation as a green source of energy.[28–30] By controlling the reaction conditions, urea-derived anions can be intercalated within the LDH structure, which could be considered *in situ* surface functionalization.[31–34] It was reported that the insertion of heteroatoms (such as nitrogen) within the catalyst structure enhances its photocatalytic activity.[15] The main target of this work is to measure the photocatalytic activity of the homogeneously precipitated Cu–Al LDH for the GHGs (CH_4, CO_2, and H_2O) conversion. To the best of our knowledge, no data have been reported for the use of homogenously precipitated Cu–Al LDH materials for this reaction previously (Table S1†).

2 Materials and methods

2.1 Materials synthesis

The chemicals used were copper(II) nitrate trihydrate ($Cu(NO_3)_2\cdot 3H_2O$, assay ≥98 wt%), aluminium nitrate nonahydrate ($Al(NO_3)_3\cdot 9H_2O$, assay ≥98 wt%), and urea (assay ≥99.5 wt%). All raw materials were purchased from Sigma-Aldrich and used without any further purification. The water used in this work was deionized using a WaterPro system (Labconco Co., USA).

In the typical synthesis, a solution of the metal salts (M^{II} = Cu and M^{III} = Al) nitrate and urea (U) mixture was suited in a 1 L three-neck glass flask (synthesis reactor). The total metal (M) concentration was 0.05 mol L^{-1}. The M^{II}/M^{III} molar ratios and urea to total metal concentration molar ratios were varied as indicated in Table 1 and Section S1.† The synthesis reactor system was illustrated in our previous work.[32] The mixture was subjected to different MW irradiation (Table 1) in the domestic MW oven, operating at a frequency of 2.45 GHz and a maximum energy of 900 watt; (Daewoo, South Korea) with continuous stirring by a mechanical stirrer (Stuart, UK). The synthesis reaction was performed under atmospheric pressure.

Table 1 Sample abbreviations with corresponding synthesis conditions

Sample code	MW power	U/M	M^{II}/M^{III}
Effect of MW power			
C1	180	10	3 : 1
C2	270	10	3 : 1
C3	360	10	3 : 1
Effect of U/M ratio			
C4	270	7	3 : 1
C5	270	5	3 : 1
C6	270	4	3 : 1
C7	270	3	3 : 1
Effect of M^{II}/M^{III} ratio			
C8	270	5	2 : 1
C9	270	3	2 : 1
C10	270	5	4 : 1

The synthesis time was fixed for all the prepared materials at 90 minutes. The temperature of the reaction was maintained at ~95 °C, and the pH of the solution was periodically measured by a pH meter model pH-213 (Hanna, USA). A bluish-green precipitate (PPT) was distinguished. The reaction was stopped immediately after the reaction time by cold water. The formed PPT was then centrifuged (MPW-352; Poland), washed several times with deionized water, and dried at 80 °C. The sample abbreviations and synthesis conditions are listed in Table 1.

2.2 Characterization

The physicochemical properties of the synthesized materials were characterized by different techniques. The crystallinity and phase identification were determined using powder X-ray diffraction (XRD) (X'Pert PRO, PANalytical, Netherlands) by Cu Kα radiation at 40 kV with a 2θ angle range from 4° to 70°, a step size of $2\theta = 0.02°$, and a scanning step time of 0.4 s. The surface functional groups were determined by Fourier Transform infrared (FT-IR) analysis (Nicolet IS 50 FTIR Spectrometer (Thermo-Fisher, USA)). The elemental analysis was performed using energy-dispersive spectroscopy (EDS) (Zeiss SmartEDX detector). The optical properties of the prepared LDH samples were examined using diffuse reflectance UV/vis spectroscopy (DR-UV/vis), GBC Cintra-3030UV visible spectrophotometer. The materials' photoluminescence (PL) spectra were recorded by Cary Eclipse Fluorescence Spectrometer equipped with Xe-lamp (Agilent, USA). The excitation wavelength was 350 nm. The material morphologies were characterized using a field emission scanning electron microscope (FE-SEM), Carl Zeiss, Sigma VP 300 (Germany).

2.3 Photocatalytic activity

The ability of the prepared catalysts towards $CH_4/CO_2/H_2O$ photoconversion under visible light in a dynamic flow system was tested. The source of visible light is an ozone-free Xenon arc lamp (150 watt), model OPS A-150 Newport Cooperation. The working power was 140 watt. In a gas-tight glass vessel reactor, 50 mg of the catalyst was mixed with 150 mL of deionized water under stirring. A flow of CH_4/CO_2 (85 : 15 vol%) was allowed to pass through the reactor in the dark for 1 h. Then, the light is turned on while the gas flow (5 mL min^{-1}) is passed. The gas concentration before and after the reaction was continuously measured by an online natural gas analyzer (Chromatec Crystal 9000, Russia). The instrument is a gas chromatograph equipped with two thermal conductivity detectors (TCD) and a flame ionization detector. The analysis columns used are Hp-1 60, MolSeive, and Carboxen 1000. To measure the product formed in the liquid phase, after the reaction time, the liquid portion was collected and transferred to the headspace vials. The liquid samples were heated in the headspace for 1 h, then the liberated gases were analyzed using headspace gas chromatography-mass spectroscopy (HS-GC-MS); Chromatec Corporation, Russia.

The light-off experiment was performed under the same conditions as the reaction but without both light illumination and catalyst. The gas mixture was continuously fed through the catalytic reactor, which held 150 mL of deionized water. The flow rate was 5 mL min^{-1}. The change in gas mixture concentrations before and after the reactor was measured.

3 Results and discussion

3.1 pH monitoring

Monitoring the pH variation during the synthesis reaction gives important information about the hydrolysis process and, consequently, the formation of the formed phases. Three different factors are considered during the synthesis of the materials under investigation: the effect of the MW power, the effect of urea percentages, and the effect of the M^{II}/M^{III} ratio (Table 1). The pH of the material synthesis solution is gradually raised by the action of the release of OH^- due to urea hydrolysis.[35] The detailed discussion of pH variation during the material synthesis reaction is listed in the ESI File in Section (S2), Fig. (S1–S4), and Tables (S2–S4).† The formation of PPT was observed when the pH exceeded the value of 4; its time depends on the reaction conditions. Thus, for the same reaction conditions, the PPT is formed earlier at a higher MW power, higher urea concentration, or high M^{III} ratio. Very low yield was noticed for samples C6, C7, and C9, with corresponding final pH values of 4.22, 4.06, and 3.92, respectively.

3.1.1 XRD analysis. The obtained XRD patterns of the as-prepared materials are shown in Fig. 1, 2a, S5, and S6.† The patterns exhibit sharp and symmetrical peaks at low 2θ angles, while broad and less intense peaks appear at higher 2θ angles. The XRD patterns for all as-prepared materials are typical of the pattern of copper–aluminium hydrotalcite-like material intercalated with carbonate anions (PDF file no. 37-0630). No individual copper, aluminium oxide, or hydroxide was detected, indicating the efficiency of the proposed synthesis parameters to produce pure LDH phases. The patterns were indexed as a rhombohedral crystal system with an $R\bar{3}m$ space group.[36,37] Thus, assuming 3R packing of the layers, *hkl* diffraction plans (003), (006), and (012) are observed at $2\theta = 12.6°$ (± 0.1), 25.4° (± 0.1), and 33.7° (± 0.1) with the corresponding basal spaces of 7.0 (± 0.1), 3.5 (± 0.1), and 33.7 (± 0.1) Å, respectively. Based on the layer thickness postulation of 4.8 Å, the interlayer gallery height can be calculated from the difference between the layer thickness and the $d_{(003)}$ spacing. The obtained interlayer gallery height was 2.2 (± 0.1) Å, is suitable for carbonate intercalation and/or oriented anions.[32,33,37,38]

The lattice parameters (a) and (C) for the LDH crystal structure are determined from $d_{(011)}$ and $d_{(003)}$, respectively. The (a) parameter corresponds to the cation–cation average distance within the brucite-like layer, thus $a = 2d_{(110)}$.[18,36] The plane (011) is the first peak of the doublet that appeared at $2\theta \sim 60°$ and is characterized by a weak and broad peak. The (a) parameter depends mainly on the effective ionic radius of Cu^{2+} (0.74 Å) and Al^{3+} (0.54 Å) and ionic charge. Increasing aluminium content causes a decrease in (a) due to the increasing layer charge density.[37] The weakening of the (110) plane is due to the presence of transition metal (Cu^{2+}), that disrupts the octahedral cation coordination and, consequently, leads to poor long-range ordering (known as the Jahn–Teller distortion effect).[27,39] It was observed that the intensity of the (110) plan decreased as the urea content decreased (Fig. 1), reflecting the role of urea percentage on the cation ordering within the layered structure. Furthermore, the (a) value decreases as the urea concentration increases, in agreement with that reported previously.[40] This could be explained as follows: at the same synthesis reaction condition, increasing urea content results in a high hydrolysis rate, and further metal precipitation gives rise to the high LDH yield rate under the MW power, as indicated from the pH curves in Fig. S2 and Table S3.† The C parameter is the distance corresponding to one brucite and one interlayer distance. It could be calculated from the d-spacing of the (003) plane, where $C = 3d_{(003)}$ is directly affected by the interlayer anion size, orientation, the electrostatic charge between the negatively charged anion and the positively charged layers, and the degree of interlayer hydration.[37,41–43]

The previously obtained results were considered for LDH phase (I) because another LDH phase (II) was detected in all the as-prepared materials at lower 2θ close to 9.9, 19.9°, and 31.9°, corresponding to (003), (006), and (012) plans with d spaces of close to 8.8, and 2.8 Å. The LDH phase (II) is in agreement with that reported previously,[44–46] and the presence of two LDH phases was reported by Peng and co-workers for the Cu–Al LDH prepared using the urea hydrolysis method (Table 2).[46] The intensity of this phase varies according to the reaction conditions. The interlayer gallery heights are close to 4.1 Å, which could be due to the intercalation of larger-dimensional anions such as urea-derived anions.[27,31] The intensity of LDH phase (II) relative to LDH phase (I) is increases as the urea percent decreases and as the Al percent increases (Table 2, Fig. 1 and 2a). For samples prepared at different MW powers, the gallery

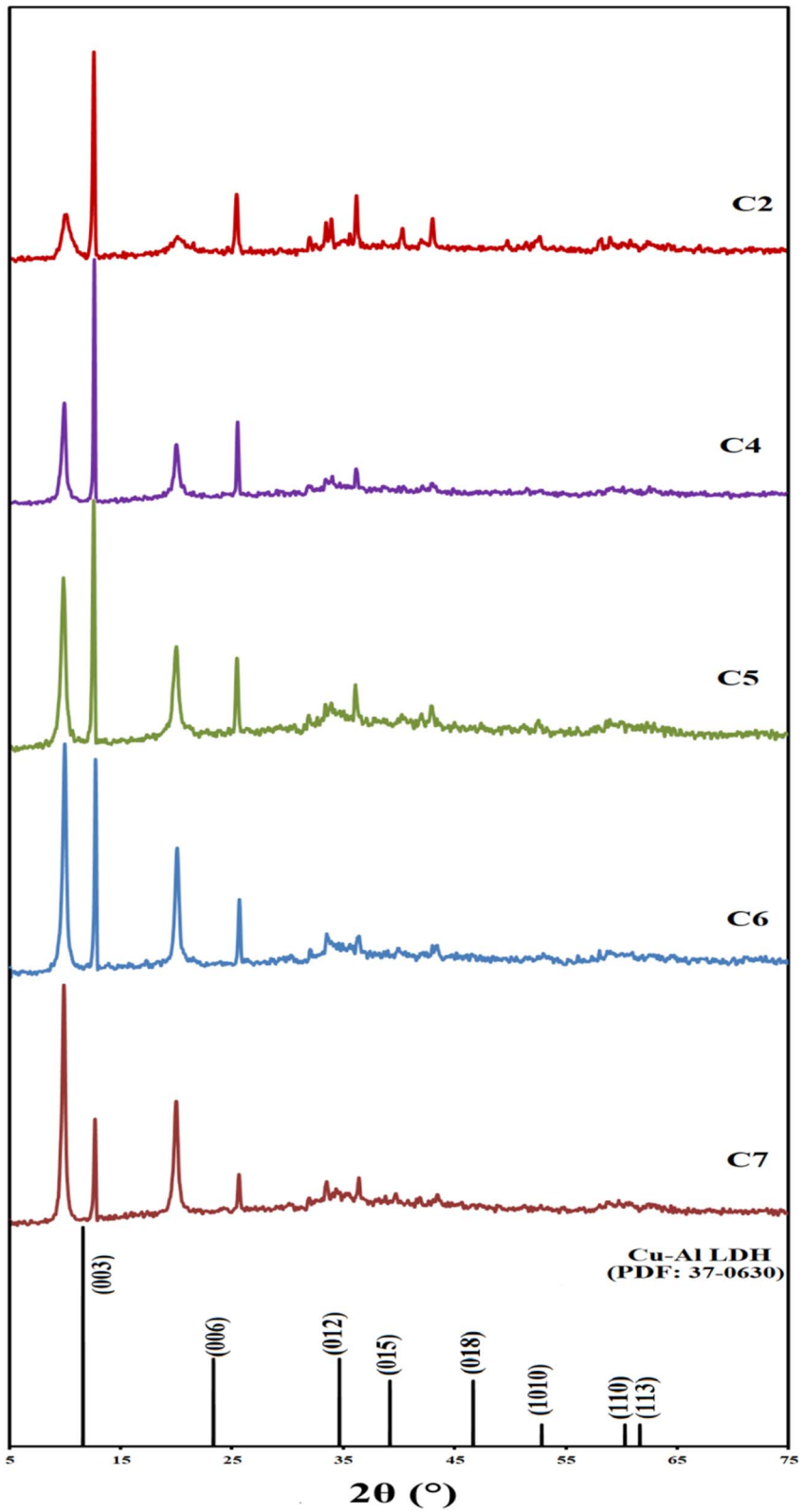

Fig. 1 Effect of varying urea concentration on the LDH phases of the prepared samples.

height of phase II increases as the MW power increases (Fig. S6†). This could be attributed to the increasing MW power that accelerated the urea hydrolysis and permitted the insertion of large amounts of the produced anions within the layers. This observation is in agreement with that observed in the plateau region (v) in the pH monitoring curve (Fig. S1†).

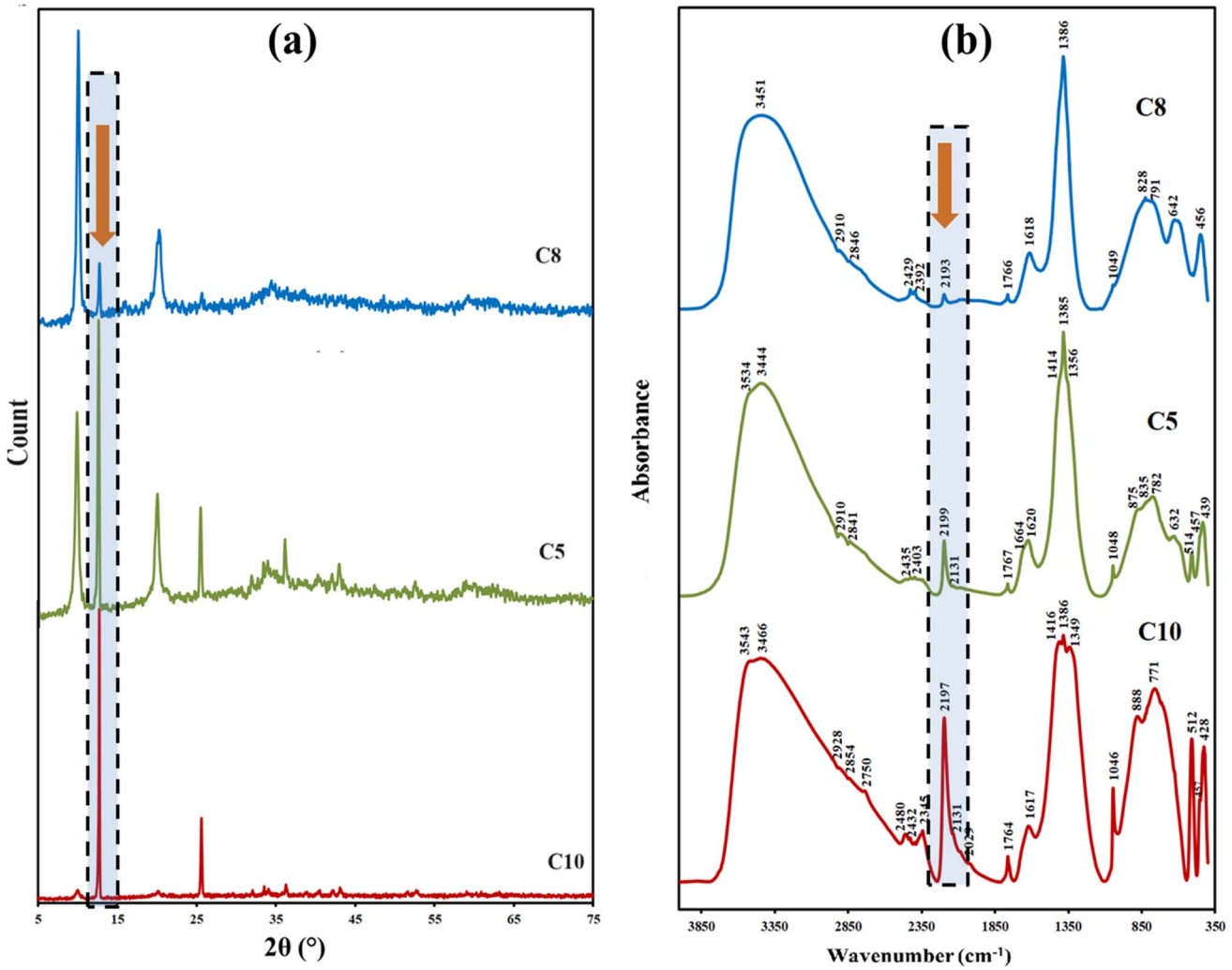

Fig. 2 (a) XRD patterns and (b) FTIR spectra of materials prepared with different M^{II}/M^{III} ratios.

Table 2 Detected LDH phases and Lattice parameters of the LDH samples

	Phase I				Phase II			
Sample	$d_{(003)}$ (Å)	a (Å)	C (Å)	Gallery height (Å)	$d_{(003)}$ (Å)	C (Å)	Gallery height (Å)	Phase (II)/phase (I) (count%)
Effect of MW power								
C1	7.072	3.048	21.215	2.272	8.274	24.823	3.474	11.393
C2	7.018	3.050	21.054	2.218	8.805	26.414	4.005	17.556
C3	7.018	3.047	21.055	2.218	8.889	26.667	4.089	12.194
Effect of U/M ratio								
C2	7.018	3.050	21.054	2.218	8.805	26.414	4.005	17.556
C4	7.009	3.078	21.028	2.209	8.879	26.638	4.079	28.748
C5	7.024	3.087	21.071	2.224	8.985	26.955	4.185	41.595
C6	6.950	3.109	20.851	2.150	8.892	26.677	4.092	51.533
C7	6.974	3.109	20.921	2.174	8.926	26.779	4.126	69.847
Effect of M^{II}/M^{III} ratio								
C9	6.955	—	20.865	2.155	8.904	26.712	4.104	73.698
C8	6.979	3.053	20.938	2.179	8.823	26.470	4.023	84.228
C5	7.024	3.087	21.071	2.224	8.985	26.955	4.185	41.595

Sample C9 was prepared under low a U/M = 3 percent and a low M^{II}/MIII = 2 ratio (Table 1). The corresponding C9 XRD pattern did not exhibit a peak at $2\theta \sim 60°$, so its lattice parameter (a) could not be calculated (Table 2). In this regard, samples C6, C7, and C9 will not be considered for further investigation because of their very low ppt yield as indicated by the pH change curves (Fig. S2 and S4†) and the low intensity of the resulting LDH phases (Fig. 1 and S5†).

3.1.2 FTIR analysis. The FTIR spectra of the prepared samples are shown in Fig. 2b, S7, and S8.† The LDH lattice characteristic vibration is observed at ~424 cm^{-1} which corresponds to the O–M–O stretching vibration within the layers.[36,42] This band is shifted to a higher wave number as the aluminium content increases to reach 456 cm^{-1}, attributed to the $[AlO_6]^{3-}$ condensed group. Furthermore, the absorption band at ~790 cm^{-1} related to Al–OH translation and shifted to a lower frequency as the copper content increased (Fig. 2b).[47,48]

A broad and intense vibrational band in the region between 3000 and 4000 cm^{-1} is attributed to the hydrogen-bonded hydroxyl groups in the brucite-like layers with interlayer water molecules.[37,46] It is characterized by two maxima with nearly the same intensities at ~3540 cm^{-1} and ~3440 cm^{-1}. As the aluminium content increased, only one maximum was distinguished at ~3455 cm^{-1} and became broader (Fig. 2b). This may suggest that the interaction between the layers, interlayer anions, and water molecules increases as the aluminium concentration increases.[49] No isolated bands in this region are observed that are characteristics of copper hydroxide or aluminium hydroxide. This indicates that all hydroxyl groups are involved in the hydrogen bonding and confirms the results from the XRD for the purity of the material's LDH structure. The interlayer bending mode appears at ~1620 cm^{-1}.[36,37]

The asymmetric stretching vibrational ν_3 mode for interlayer mono-dentate carbonate has appeared at the absorption band ~1383 cm^{-1}. The splitting of this peak, observed at ~1350 cm^{-1}, could be attributed to the lowering of the symmetry of carbonate anions. This indicates the different intercalation modes of bi-dentate carbonate. Another split shoulder is detected at ~1410 cm^{-1}, and it becomes more distinguished as the copper content increases. This band could be related to the ν_3 mode of interlayer-free carbonate anions.[31,50] The carbonate ν_1 mode is detected as a small band at ~1045 cm^{-1}. This vibrational mode is IR inactive; however, the existence of the carbonate anions in the interlayer structure is affected by the electrostatic interaction with the positively charged layers and interlayer water molecules. This leads to the lowering of its symmetry; consequently, this mode becomes an IR active.[36,37,42] The absorption band at ~880 cm^{-1} is assigned to ν_2 carbonate deformation mode.[51] The small absorption bands at 2300 to 2480 cm^{-1} could be due to the physically adsorbed CO_2 on different surface-accessible sites.

The absorption band that appeared at ~2198 cm^{-1} could be attributed to the intercalated n-bonded isocyanate group.[29,51] This band decreased as the copper content decreased (Fig. 2b). This reflects the role of metal type in the urea hydrolysis reaction rate and, consequently, the type of the produced urea-derived anion. The very small shoulders at ~2131 and 2090 cm^{-1} could be an indication of the different intercalated modes of the isocyanate groups.[52,53] The small band at ~630 cm^{-1} could be due to the bending vibration of NCO.[53,54] This band is not distinguished in LDH samples with high aluminium content. The sharp and small band at ~512 cm^{-1} is found to increase with copper content (Fig. 2b), which may be due to the bending vibration of the C–N bond.[55] By comparing the results from the IR spectra and XRD patterns of samples prepared at different M^{II}/M^{III} ratios (Fig. 2a and b; in the shaded region under the arrows), it was observed that the intensity of the absorption band related to the isocyanate group (at ~2198 cm^{-1}) is directly proportional to the intensity of the XRD peak at 2θ~ 12.6° (d ~7.0 Å). As the isocyanate IR absorption band increases, the intensity of the diffraction peak at $2\theta \sim 12.6°$ increases. According to the reference material data (PDF file no. 37-0630), this d spacing is for the presence of intercalated carbonate anions. From the above results, it could be concluded that the d spacing (~7.0 Å) of the prepared Cu–Al LDH materials is suitable for the intercalation of carbonate anion and oriented isocyanate groups. The intercalated anions in the interlayer space could be oriented in order to maximize the interaction with the positively charged layers.[56]

The appearance of shoulders at ~2900 and 2830 cm^{-1} may indicate the hydrogen-bonded bridging water molecule with carbonate and NH vibration.[57] The small shoulder that appeared at ~1666 cm^{-1} could be assigned to the C=O group in the amide group (–CO–NH–).[54,58,59] The presence of NHCOO– species is supported by the small vibrational band at ~1764 cm^{-1}. This band becomes sharper and more intense as the copper content increases.[58,60] In addition, the band maximum is at ~3444 cm^{-1} and shifts to a higher wavenumber as the Cu content increases.[61,62] This could be assigned to the hydrogen-bonded stretching NH groups. These results are in agreement with the XRD data. Thus, the intercalation of bi-dentate carbonate anions and oriented isocyanate species inside the layered structure could be responsible for the d_{003} spacing of 7.0 (±0.1) Å. Moreover, the d_{003} spacing of ~9.9 Å could be suitable for the intercalation of bigger urea-derived anions.[31]

The EDX analysis also confirmed the presence of nitrogen-containing groups. Fig. (S9) and Table (S5)† represent the EDX analysis and elemental atom percent results of sample C4. This is in agreement with the pH change observation, XRD, and FTIR data. The results confirm the theoretical metals percentage ratio (Cu : Al = 3 : 1).

3.1.3 DR UV-vis analysis. The photocatalytic activity depends on the optical properties of the catalysts.[63] Based on the diffuse reflectance results, the Kubelka–Munk (K–M) function $F(R_\infty)$ can be calculated with the absorbance equivalence spectrum:[64]

$$F(R_\infty) = \frac{K}{S} = \frac{(1 - R_\infty)^2}{2R} = \propto \quad (1)$$

where, K and S are the absorbance and scattering (K–M) coefficients, R_∞ is the reflectance R of an infinitely thick specimen $R_\infty = \frac{R_{\text{sample}}}{R_{\text{standerd}}}$, and $\propto$ is the absorption coefficient.

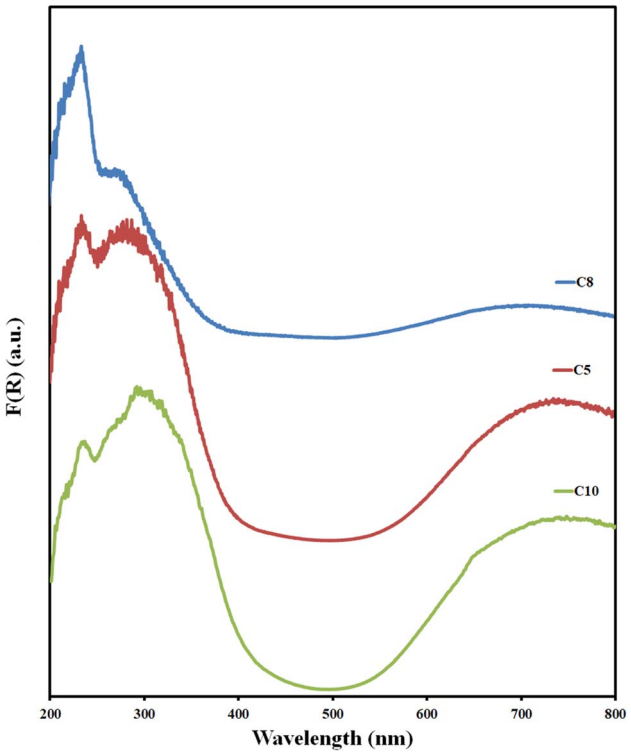

Fig. 3 DR UV-vis spectra for samples prepared at different M^{II}/M^{III} ratios.

The characteristics of the DR UV-vis spectra analysis of the prepared Cu–Al LDH materials are represented in Fig. 3 and S10,† where a plot of Kubelka–Munk (K–M) function $F(R_\infty)$ *vs.* the wavelength is shown. The spectra indicate the presence of three absorption edges in the regions 200–250 (I), 250–400 (II), and 600–800 nm (III) as follows:

1- In region I, absorption edges ~233 nm (intense peak), its intensity increases as the MW power increases; decreases with aluminum content; and is slightly affected by the change in urea concentration. This band has not been detected previously in typical Cu–Al-LDH materials.[42] This band could be due to the type of intercalated anion that contains a nitrogen group, where the presence of nitrogen in the catalyst structure enhances its optical properties.[65–67]

2- Region II is a broad shoulder with an absorption edge of ~275 nm, whose intensity decreases with increasing MW power. It becomes more distinct with increasing copper content and is slightly shifted to a lower wavelength with increasing urea concentration. This band may be due to the $O^{2-} \rightarrow Cu^{2-}$ ligand-to-metal charge transfer transition.[37,42,68]

3- Region III, a very broad peak at ~730 nm, has an intensity that decreases with increasing MW power and increasing urea concentration. This band could be attributed to the d–d transition $^2Eg(D) \rightarrow {}^2T_{2g}(D)$ of the $Cu^{2+}(d^9)$ distorted octahedron due to the Jahn–Teller effect.[37,42,49] Regarding the M^{II}/M^{III} ratio, the band gap is decreasing with increasing Cu (d^9) content. This indicates a decrease in the d–d transition energy barrier.[69]

The energy band gap (E_g) was calculated using the Tauc method[67,68,70] (Section S3†).

Multiple band gaps have been observed in the plot of the (K–M) function with the photon energy, with the main band gap (I) at ~3.0, band gap (II) at ~1.2, and band gap (III) at ~4.00 (eV); Fig. (S11–S13).† The fit of their values to the Tauc model is listed in Table 3.[71] The multi-band gaps were reported previously.[51,72,73]

The DR UV-vis results demonstrate that the Cu–Al LDH materials could be regarded as visible light photocatalysts[69] when compared with the results reported previously.[74] Additionally, it might have potential uses as semiconductors in photosystems (like solar cells) or photochemistry.[51]

3.1.4 Photoluminescence analysis. Photoluminescence analysis is a non-destructive and highly sensitive technique used to indicate the material's structural characteristics through the determination of its surface active sites. It may give

Table 3 The Cu–Al LDH calculated energy band gap

	Band (I)			Band (II)			Band (III)		
		Fit to $(\propto h\nu)^{1/n}$			Fit to $(\propto h\nu)^{1/n}$			Fit to $(\propto h\nu)^{1/n}$	
Material	Extrapolated E_g (eV)	$n = 2$	$n = 1/2$	Extrapolated E_g (eV)	$n = 2$	$n = 1/2$	Extrapolated E_g (eV)	$n = 2$	$n = 1/2$
Effect of MW power									
C1	2.7	2.9	3.3	1.2	1.2	1.4	4.2	4.4	4.75
C2	3.1	3.2	3.5	1.2	1.3	1.5	4.15	4.3	4.6
C3	2.6	2.9	3.1	1.1	1.2	1.4	4.5	4.6	4.9
Effect of urea concentration									
C2	3.1	3.2	3.5	1.2	1.3	1.5	4.15	4.3	4.6
C4	3	3.1	3.3	1.1	1.2	1.3	3.35	3.7	4.3
C5	3.1	3.15	3.4	1.05	1.1	1.3	3.3	4.7	4.4
Effect of M^{II}/M^{III} ratio									
C8	3.2	3.2	3.7	1.2	1.2	1.4	4.4	4.5	4.7
C5	3.1	3.15	3.4	1.05	1.1	1.3	3.3	4.7	4.4
C10	2.9	2.95	3.2	1.05	1.1	1.3	3.3	3.6	4.4

information about the nano-sized semiconductors' surface charge carriers, surface defects, and oxygen vacancies. In addition, the PL emission is directly related to the free carriers' recombination rate and, consequently, the efficiency of the photocatalytic process.[75,76] To the best of our knowledge, there is no available data considering the PL analysis of Cu–Al LDH prepared by urea hydrolysis.

Fig. 4 shows the photoluminescence spectra of the prepared samples when excited at 350 nm. All samples exhibit four PL emission peaks in the visible region. Fig. 4a shows the detailed peaks taken from sample C3 as an example. The detected peaks were at ~426 (small and broad peak), 483 (small shoulder), 499 (sharp and intense peak), and 520 nm (small and broad peak). The main cause of this activity is the presence of surface defects and surface-trapped charge carriers (excitons).[77] This emission could be attributed to the charge-transfer transition of the electrons trapped in the oxygen vacancies that are considered photo-induced electron–hole (e^-–H^+) recombination centres.[78] The most intense peak at 499 nm may be a result of emission generated by localized surface-trapped charge carriers recombination.[79] These results reveal the presence of multiple energy levels responsible for Cu–Al LDH materials luminescence activity.[80] The results also confirmed the data obtained from the DR-UV/vis analysis.

The lower PL intensity is an indication of longer charge separation and, consequently, a lower recombination rate of photogenerated electrons and holes that are formed during the excitation process.[81,82] Gevers and co-workers have demonstrated that there are several reasons for the LDH luminescence emission broadening, such as:[83]

- Surface defects result from layer stacking disorder, edges and surface sites, oxygen, and cation vacancies.

- The unique LDH structure permits excitons to be generated within the interlayer and interlayer formations.

- Excitons that are stabilized by the Al^{3+} cation islands within the layers.

- The presence of interlayer anions assists the holes' stabilization, resulting in lowering the emission energy. This may cause the PL peak to broaden.

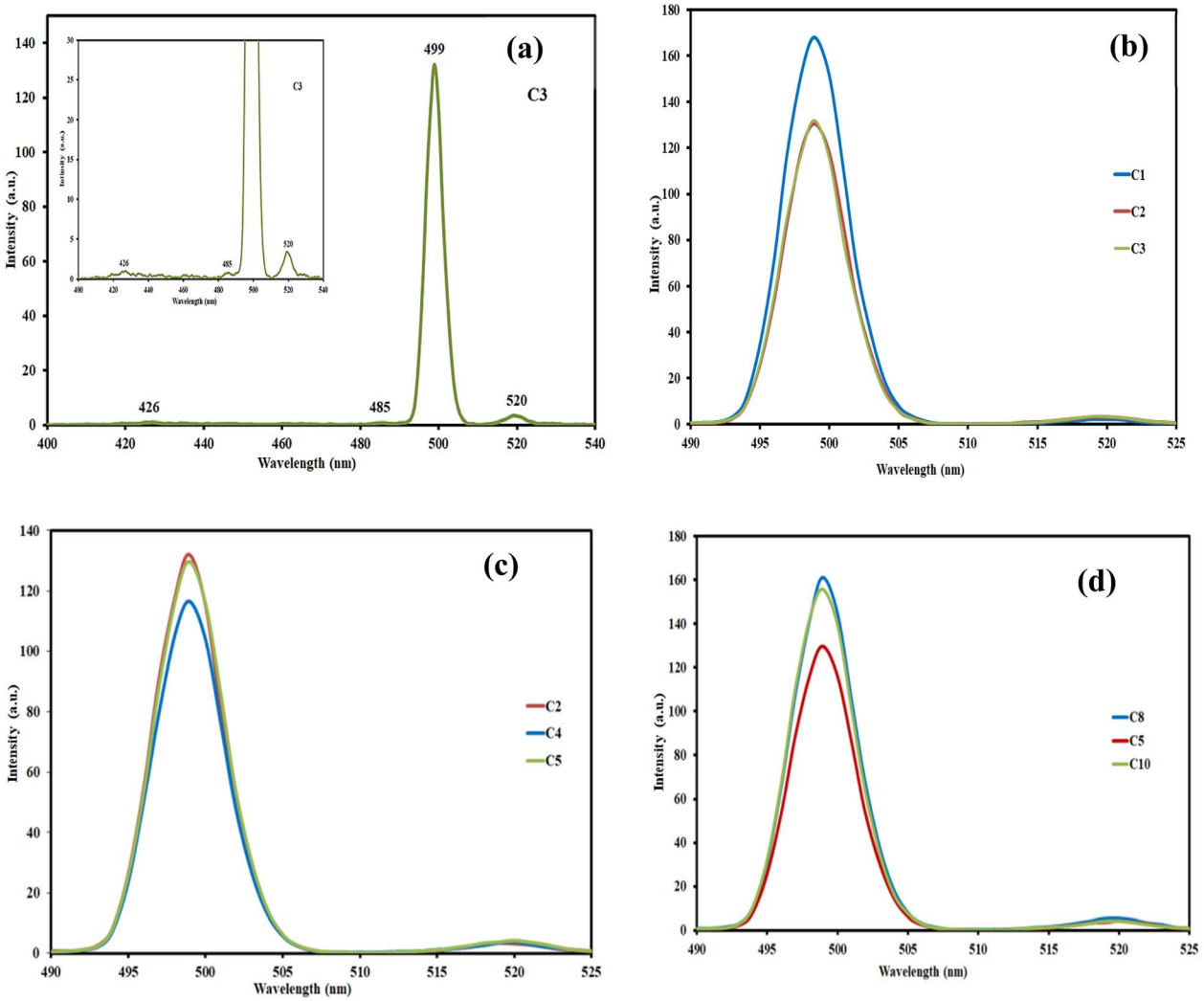

Fig. 4 Photoluminescence spectra of (a) sample C3, (b) samples prepared at different MW power, (c) samples prepared at different urea concentrations, and (d) samples prepared at different M^{II}/M^{III} ratios.

The insertion of nitrogen-containing groups (resulting from urea degradation or intercalated amino groups) may maximize the hole stabilization process, thus enhancing the LDH optical, as reported previously.[78,84–86] Regarding the effect of urea concentration (Fig. 4c), the C4 sample, with U/M = 7, represents the lowest intensity of the main peak (at ~499 nm). The M^{II}/M^{III} ratio variation (Fig. 4d) revealed that C5, with $M^{II}/M^{III} = 3$, had the lowest intensity. This observation is in agreement with that reported previously.[87] For the samples prepared at different MW power, power at 270 and 360 watt (C2 and C3) shows a comparable intensity (Fig. 4b).

3.1.5 FE-SEM analysis. The morphology of the prepared Cu–Al LDH materials was examined by FE-SEM. The images reveal the presence of nanoparticles; their size depends on the synthesis conditions. The morphology of the prepared Cu–Al LDH materials was examined by FE-SEM. The images reveal the presence of nanoparticles; their size depends on the synthesis conditions. Regarding the Cu–Al LDH that was prepared under different MII/MIII ratios, C8 with high aluminium content exhibits spherical aggregates with the lowest particle size (~6–30 m) (Fig. 5a). It was observed that, as the copper content increases, the particle size increases, forming sheet-like particles of large size (Fig. 5C). Increasing the urea content slightly increases the average particle size (~40–100 nm) (Fig. S14†), while increasing the MW power decreases the average particle size (~30–100 nm) (Fig. S15†).

3.1.6 Photocatalytic activity. We examined the ability of the prepared Cu–Al LDH photocatalysts to convert GHGs (CH_4, CO_2, and H_2O) under visible light into valuable products. The reaction is performed in a glass reactor *via* a dynamic gas flow system at room temperature and under atmospheric pressure. Fig. (6) illustrates the variation of CH_4 and CO_2 conversion percent during the photochemical reaction using the prepared Cu–Al LDH catalysts. The lowest conversion percentages were ~28.5 and ~11.5 for CH_4 and CO_2, respectively.

Fig. S16† represents the comparison between the conversion percentages of CH_4 and CO_2 for all the catalysts prepared at different conditions, respectively. It is obvious that, although both CH_4 and CO_2 are converted to some extent, both gases interact differently with the catalyst surface along the reaction time.

Fig. 7, S17, and S18† illustrate the cumulative converted amounts of both CH_4 and CO_2 over time under the reaction conditions as well as the selectivity of formaldehyde production. The remaining sample fractions were caused by the synthesis of more highly oxygenated hydrocarbons, and the

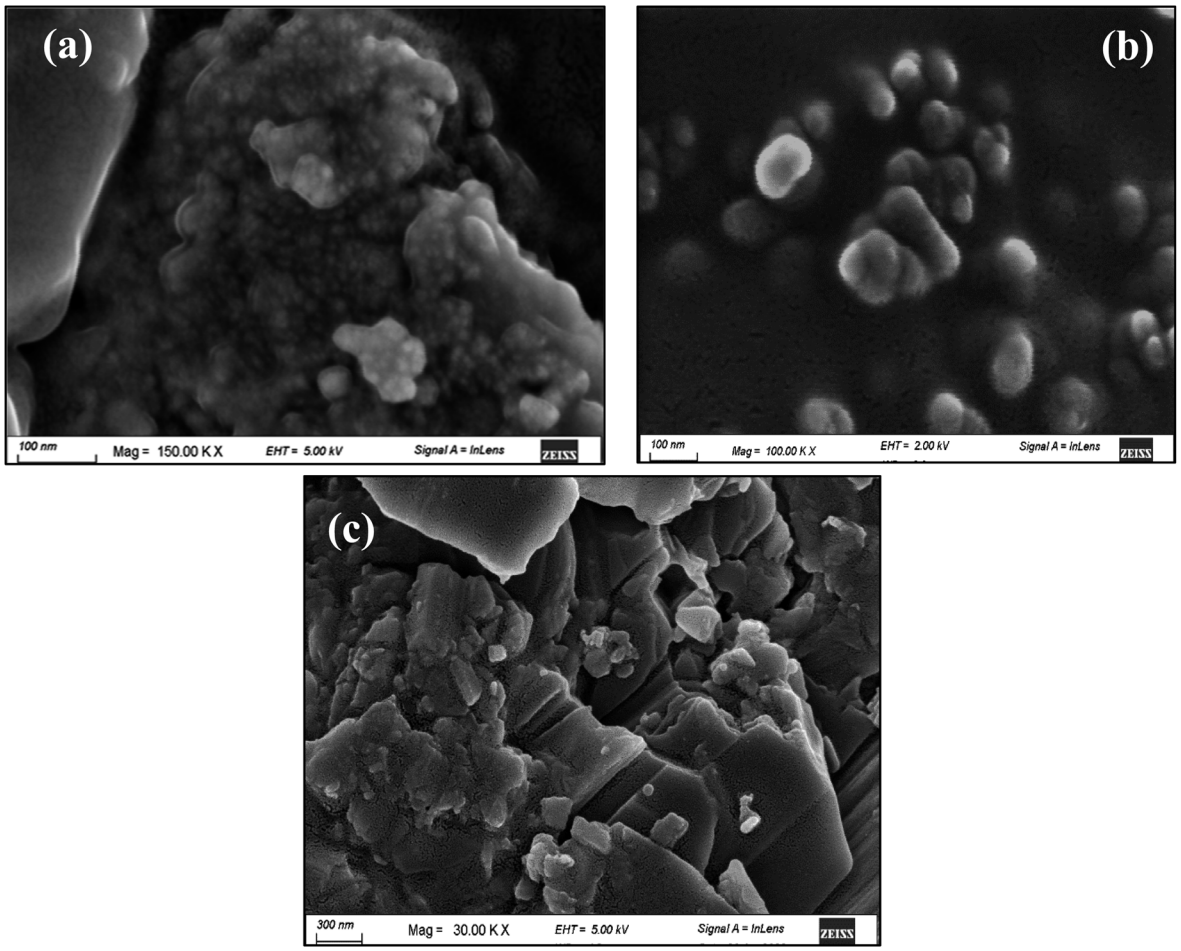

Fig. 5 FE-SEM images for (a) C8, (b) C5, and (c) C10 Cu–Al LDH materials that are prepared at different M^{II}/M^{III} ratios.

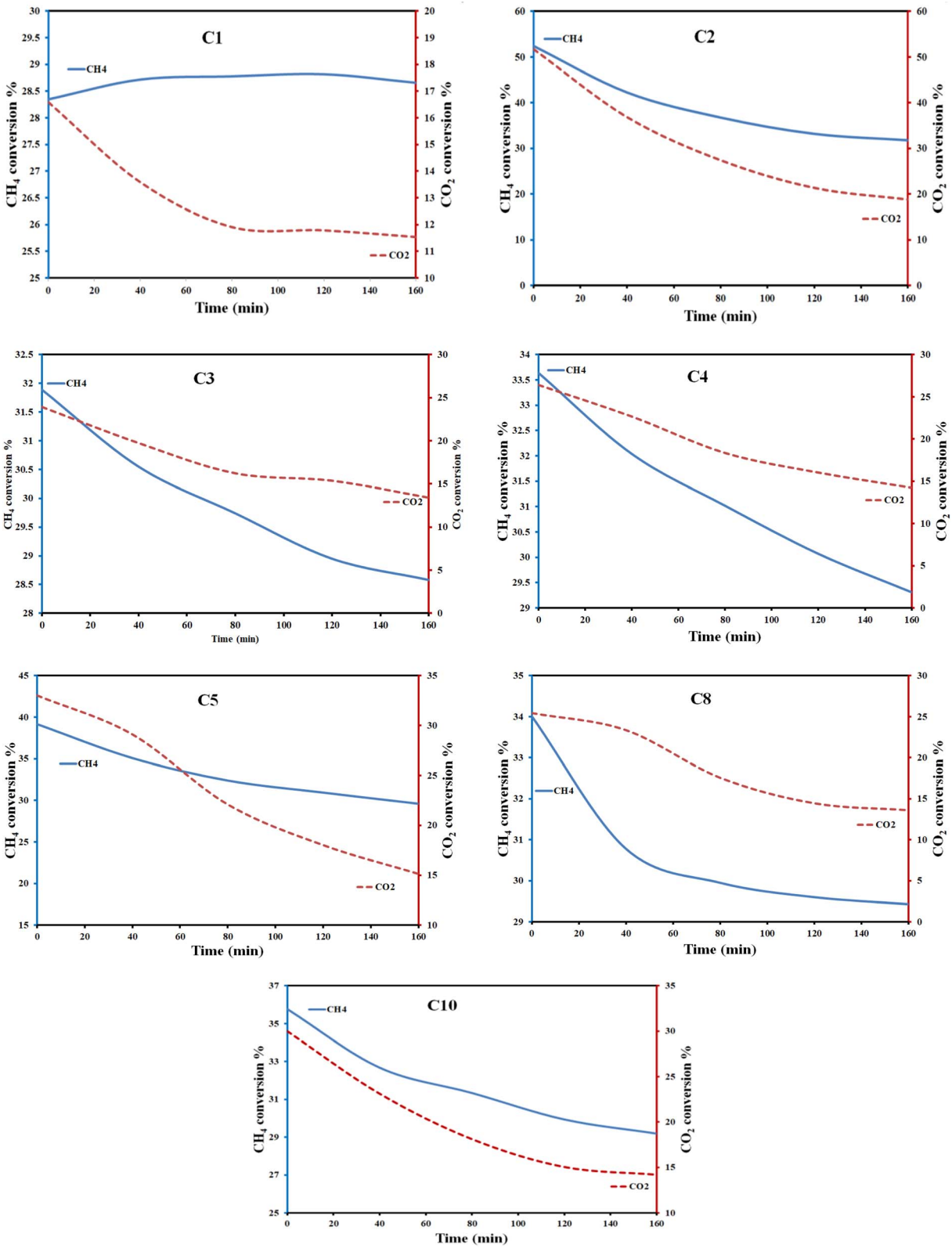

Fig. 6 Variation of CH_4 and CO_2 conversion percent under the photo reaction conditions using the Cu–Al LDH catalysts.

formaldehyde selectivity was greater than 99%. It was observed that, regarding the samples prepared at different MW power, the C2 sample converted a higher amount of CH_4 (7.47 mmol mL^{-1} g^{-1}) and CO_2 (1.02 mmol mL^{-1} g^{-1}); however, the selectivity for formaldehyde is higher with the C3 sample (Fig. 6). Compared to samples prepared at different urea

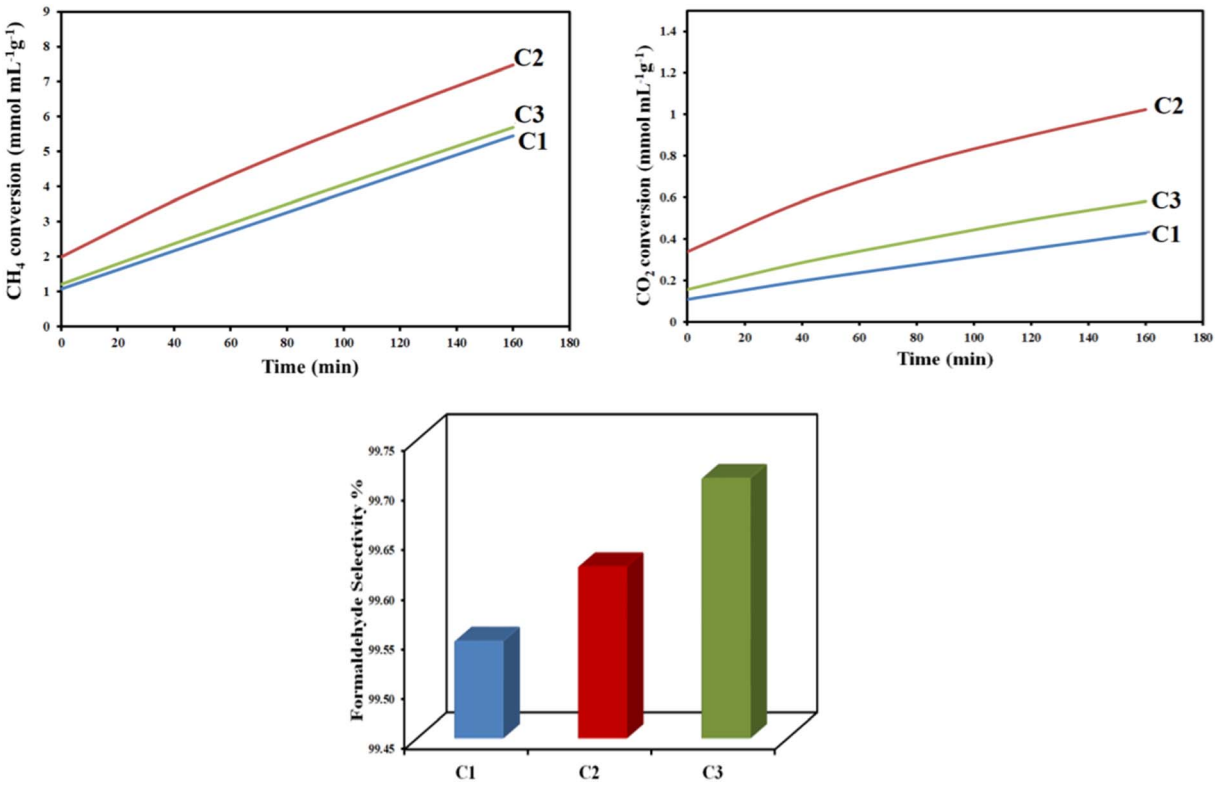

Fig. 7 Accumulative converted amounts of CH_4 and CO_2 with time and corresponding formaldehyde selectivity% using the Cu–Al LDH catalysts prepared at different MW power.

concentrations, the C2 sample with a higher urea ratio was observed to convert a higher amount of CH_4 and CO_2, Fig. S15.† For samples prepared at different M^{II}/M^{III} ratios, sample C5, with $M^{II}/M^{III} = 3:1$ represents the highest conversion activity and the highest formaldehyde selectivity percent (Fig. S16†).

We selected sample C4 to study the effect of increasing the catalyst dose and the effect of cycling under repeated light on/off. Fig. 8 shows the variation of CH_4 and CO_2 conversion% with the catalyst dose (0.05, 0.1, and 0.5 g catalyst). The data shows that the higher dosage results in a low conversion rate. The behaviour of methane conversion is different at a low catalyst dose (0.05 g). For higher catalyst doses (>0.05 g), the conversion starts with a low percentage, increases with time, and decreases again. In addition, the selectivity percentage of formaldehyde was higher with the low catalyst dose of 0.05 g than with the higher doses of 0.1 and 0.5 g (Fig. S19†). Increasing the catalyst dose will result in particles crowding in the solution; thus, it could suffer from the light shielding effect. In this case, the particles cannot absorb light, resulting in less conversion and less selectivity. This behaviour indicates the essential role of the catalyst in the conversion process.[88]

It was reported that the high H_2O/CO_2 ratio could lead to the formation of products such as formaldehyde, methanol, or formic acid in the liquid phase.[89] Furthermore, regarding CH_4 photoconversion, Wei *et al.* found that increasing water could be considered an effective strategy to enhance formaldehyde selectivity.[90] The high amount of water promotes catalyst dilution and enhances light absorption.[88,91] Moreover, the presence of the formed formaldehyde molecules on the catalyst surface will increase their chance of being oxidized to form CO_2. However, the excessive water amount assists the formaldehyde desorption from the catalyst surface, consequently suppressing its oxidation.[88,92] The detection of formaldehyde as a product is affected by its adsorption strength on the catalyst surface. If it is strongly bound to the surface, it is hard to detect.[93]

We tested the change in concentration of the gas mixture in the dark, where the gas flowed through the reactor system at the same conditions as the reaction but without using both light illumination and a catalyst (Fig. S20†). A small variation in the gas concentration is observed compared with the initial gas concentration value (before the catalytic reactor). This variation may be attributed to the diffusivity of both CH_4 and CO_2 in water.[94]

The durability of the Cu–Al LDH catalyst is shown in Fig. (9). Before each cycle, the light is turned off, and the gas flow is passed through the system in the dark for about 1 h before the light is turned on again. The conversion rate is enhanced after the first cycle. The minimum conversion percentage for both CH_4 and CO_2 is nearly constant in the repeated cycles. This behaviour could be related to the slow recombination rate of photogenerated electrons and holes during the excitation process by the incident light, as confirmed by the PL results. These results reflect the stability of Cu–Al LDH as the preferred photocatalyst for GHGs conversion. In addition, the presence of

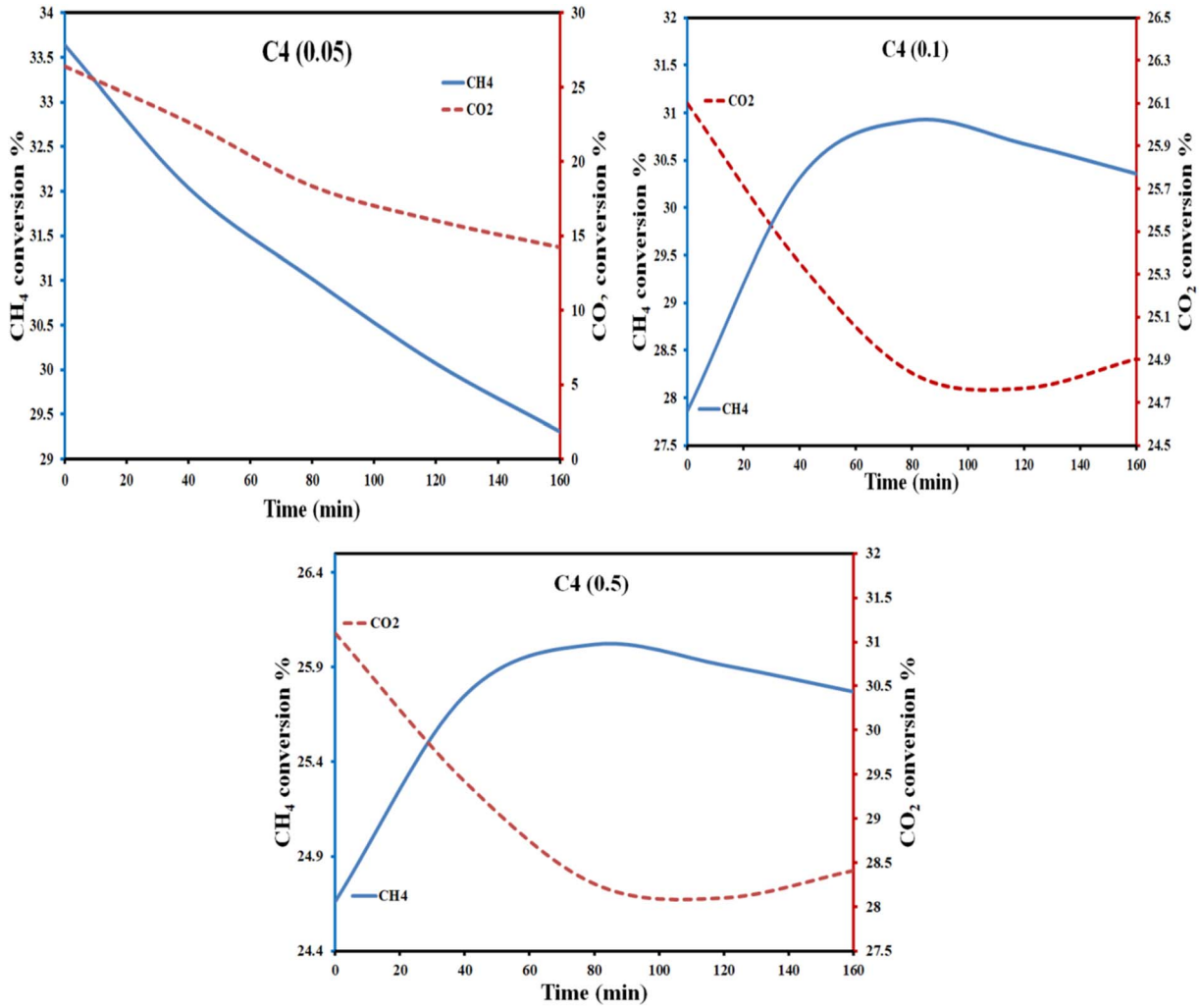

Fig. 8 Effect of C4 catalyst dose (0.05, 0.1, and 0.5 g) on the variation of CH_4 and CO_2 conversion percent under the same photo reaction conditions.

water molecules could play an important role in activating the active sites, preventing coke formation on the catalyst surface, and increasing the stability of the catalyst over time.[95–97]

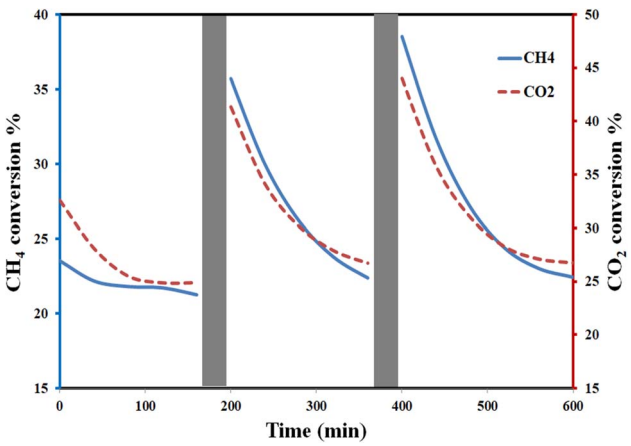

Fig. 9 Variation of the CH_4 and CO_2 conversion% in the light on/off repeated cycles.

3.1.6.1 Reaction mechanism. On the excitation of LDH by visible light, photons are absorbed with energy near the LDH band gap. The proposed reaction mechanism is illustrated in Scheme 1. The holes (h^+) and photon-generated electrons (e^-) are produced as a result of the movement of the excited electrons from the valence band to the conduction band.[74]

$$LDH + h\nu \rightarrow h^+ + e^- \quad (4)$$

The O atoms in the hydroxyl group function as the focal point of photogenerated holes in the LDH photocatalysts (formed in the (003) phase surface (*)). The holes facilitate the oxidation of water molecules that are hydrogen bonded to the hydroxyl groups of the layers.[69]

$$H_2O + * \rightarrow *OH + H^+ + e^- \quad (5)$$

$$*OH + H_2O \rightarrow *H_2O_2 + H^+ + e^- \quad (6)$$

$$*H_2O_2 \rightarrow *OOH + H^+ + e^- \quad (7)$$

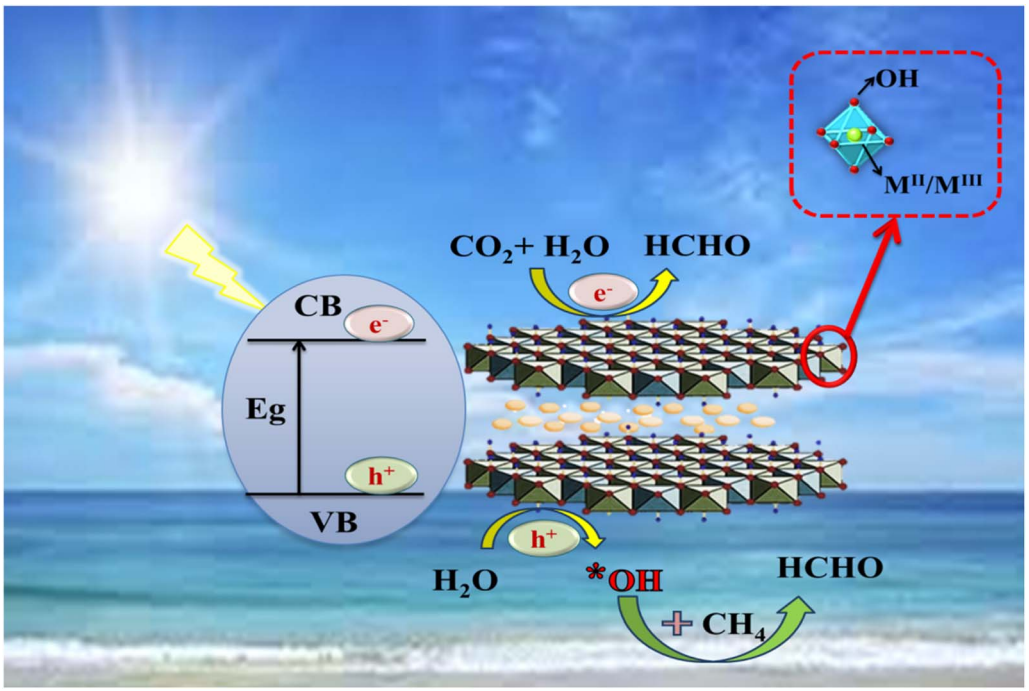

Scheme 1 Proposed reaction mechanism of photoreforming greenhouse gases by Cu–Al LDH under visible light illumination.

$$*OOH \rightarrow * + O_2 + H^+ + e^- \quad (8)$$

The main product in this work was formaldehyde (as obtained from the GC-MS analysis), which could be formed as a result of CO_2 and CH_4 conversion. The mechanism of the reaction is uncertain; however, it could be as follows:

a- During CO_2 reduction, CO_2 is first introduced to water in the dark before light illumination, thus forming the carbonic acid specie. Then, upon illumination, CO_2 could be reduced to formaldehyde:[74]

$$(Dark)\ CO_2 + H_2O \rightarrow HCO_3^- + H^+ \quad (9)$$

$$(Light)\ HCO_3^- + 2H^+ + 2e^- \rightarrow HCO_2^- + H_2O \quad (10)$$

$$CO_2 + e- \rightarrow {}^{\bullet}CO_2^- \quad (11)$$

$${}^{\bullet}CO_2^- + H_2O \rightarrow HCO_2^{\bullet} + OH^- \quad (12)$$

$$HCO_2^{\bullet} + e^- \rightarrow HCO_2^- \quad (13)$$

$$HCO_2^- + 2H^+ + 2e^- \rightarrow HCHO + OH^- \quad (14)$$

b- During methane oxidation, methane is not soluble in water,[98] so it is not affected by the surrounding water in the dark. The mechanism could be predicted as follows:

• The superoxide ($^{\bullet}O_2$) that is generated from the absorption of the photogenerated electron by the oxygen on the layer's surface subsequently forms the HOO* radical (eqn (7)), then the hydroxyl radical ($OH^{\bullet}$). Furthermore, the $OH^{\bullet}$ radical can be produced from the reaction of photogenerated holes with water molecules. The presence of such species (*OH or $*O_2^-$) could accelerate CH_4 activation by breaking the $^{\bullet}$C–H bond and forming the CH_3 radical.[68,99,100] It was stated that, due to the low reactivity of methane, the mobile $OH^{\bullet}$ radicals could be more favourable for CH_4 activation than the trapped radicals in the photogenerated holes.[99] The produced $^{\bullet}CH_3$ could be stabilized by the presence of nitrogen-containing groups on the catalyst surface.[101]

• The OH radical, considered an active oxidant, reacts with $^{\bullet}CH_3$ once formed, and one of the products may be formaldehyde.[102–104] It could be produced through the formation of the methoxy group ($-OCH_3$) which is further oxidized by the active O^- species to methanediol ($HOCH_2OH$), then dehydrated to formaldehyde (HCHO).[88,90,105,106]

• The $^{\bullet}CH_3$ radicals could be the source of the coupling products where higher hydrocarbons may be formed.[101]

In this work, a small amount of carbon monoxide (CO) was detected in the gas phase by GC-MS. This is in agreement with that reported previously, where the presence of excess water has a positive impact on the reduction of CO_2 to CO.[107] No formic acid or methanol was detected during the photoreaction in the gas or liquid phases. Moreover, higher hydrocarbon oxygenates such as ethanediol, glycolaldehyde, and acetaldehyde have been detected as small products in the liquid phase by GC-MS. This confirms the presence of a coupling reaction and may suggest the glyoxal mechanism, where the CHO radicle could be formed during the photo-excitation process.[93]

The introduction of nitrogen-containing groups within the catalyst structure increases its photocatalytic activity.[108–110] The presence of urea-derived anions in the prepared Cu–Al LDH is believed to assist in the stabilization of the CO_2 within the Cu–Al LDH structure. Thus, it allows a higher chance for conversion

Table 4 Some previously reported CO_2 and/or CH_4 photoconversion using LDH catalysts

Catalyst	Reactor	Light source	Reaction conditions	Reactant	Analysis method	Product	References
Cu–Al LDH intercalated with urea derived anions	Homemade gas-tight glass flow reactor	Solar simulator (150 W xenon lamp)	Dynamic flow system at room temperature	$CH_4/CO_2/H_2O$	• Online-gas chromatography (FID/TCD) • Headspace gas chromatography-mass spectroscopy (HS-GC-MS)	Formaldehyde (direct formation)	This work
TiO_2/Co–Al LDH	Cylindrical glass reactor	300 W xenon lamp	15 °C	CO_2 (99.9%) bubbled in water	Gas chromatography	CH_3OH/CH_4	113
Mg–Al LDH	Stainless steel cylindrical reactor with a quartz window at the top	Solar simulator (150 W xenon lamp)		0.05 mL min^{-1} CO_2 for 30 min	Gas chromatography (TCD/FID)	CO/CH_4	89
Noble metal (Pt, Pd, Au) loaded Zn–Cr LDH	Top-irradiation-type quartz glass vessel	UV irradiation from 200 W Hg–Xe lamps	Room temperature	CO_2 gas (99.995%) with water vapor	Gas chromatography (FID)	CO	114
Zn–Cu–Al/Ga LDH	Flat bottom of the quartz reactor	UV-visible light from the 500 W xenon arc lamp	32–40 °C	(2.3 kPa) CO_2/(21.7 kPa) H_2	Online-gas chromatography (TCD)	Methanol	71 and 115
Zn–Cu–Al/Ga LDH	Pyrex glass plate	UV-visible light from the 500 W xenon arc lamp	High pressure (0.4 MPa)	CO_2/H_2 (3 : 7 v/v)	Gas chromatography (TCD)	Methanol	116
Mg–In LDH	Closed circulating system with a quartz glass ceiling for illumination	UV irradiation from 200 W Hg–Xe lamp		CO_2/H_2O	• Gas chromatography (TCD) • Mass spectroscopy	CO/O_2	117
Fluorinated Mg–Al LDH and Ni–Al LDH	Quartz inner-irradiation type reaction vessel	UV irradiation from 400 W high-pressure Hg lamp	NaCl solution scavenger	CO_2/H_2O	• Gas chromatography (TCD) • Gas chromatography-mass spectroscopy (GC-MS)	CO	118
Calcined Mg–Co LDH	Quartz vessel	UV irradiation from 300 W Xe lamp	Under vacuum	0.13 MPa CH_4/H_2O	• Gas chromatography (TCD) • Gas chromatography-mass spectroscopy (GC-MS)	Coupling product (C_2H_6)	119
Ni–Al LDH intercalated with Cl anion	Quartz glass reactor	400 W high-pressure Hg lamp	Contentious flow system/35 °C	CO_2/NaCl solution	Barrier discharge ionization detector gas chromatography (BID-GC)	CO	97
Cu–Al based LDH (Cu–Mg–Al LDH, Cu–Zn–Al LDH and Cu–Ni–Al LDH)	Gas-tight system	Visible light irradiation from 500 W Xe lamp	25 °C/aA gas pump is used to accelerate gas diffusion	CO_2/H_2O	Gas chromatography (TCD/FID)	Methanol through the intermediated product (formaldehyde & formic acid)	74
ZnO@Cu–Zn–Al LDH	Quartz glass reactor	UV-visible irradiation from 450 W Xe lamp	25 °C. After 60 min the reaction vessel was heated up to 200 °C	CO_2 (30 mL min^{-1})/H_2O	Gas chromatography (FID)	CH_4	120

reaction during the catalyst excitation through the formed active species (trapped electrons and formed hole) (PL discussion).[111]

To the best of our knowledge, the conversion of GHGs (CH_4, CO_2, and H_2O) using Cu–Al LDH papered by a homogenous precipitation process was not reported previously. Also, this work represents the direct formation of formaldehyde with high selectivity using Cu–Al LDH without using a scavenger substance under normal temperature and pressure conditions, which has not been reported previously. It is worth noting that the photoconversion of GHGs to fuel without using sacrificial scavengers is considered an approach to "green chemistry".[15,16,112] Table 4 illustrates the previously reported date for using the LDH photocatalyst in CO_2 and/or CH_4 conversion in comparison with the current work.

Industrially, formaldehyde is a value-added product. It has many potential applications, such as being the raw material for the synthesis of oxymethylene ether (OME) compounds (used for combustion fuels), fuel additives, or alternative liquid fuels. Also, it can be used as a liquid organic hydrogen carrier (LOHC) in hydrogen fuel cells.[121–123] In this work, GHGs are converted to value-added products by utilizing visible light energy (as a green chemistry approach) using a low-cost, environmentally friendly photocatalyst.

4 Conclusion

Anthropogenic activity results in the accumulation of GHGs in the atmosphere, consequently causing global warming phenomena that have a detrimental effect on the environment and health systems. Utilization of GHGs (especially CO_2, CH_4, and H_2O) to produce value-added material is considered a way to reduce their accumulation in the atmosphere. In this work, we aimed to convert these gases using a photo-efficient catalyst under visible light.

Due to their distinctive structural characteristics, layered double hydroxide (LDH) materials have inspired us. So, we have successfully homogenously precipitated Cu–Al LDH by urea hydrolysis under MW irradiation. The effects of MW power, urea concentration, and aluminium content percent were studied. Controlling the reaction conditions allows the intercalation of the urea-derived anions within the layer structure. These nitrogen-containing anions enhanced the optical properties of the prepared nano Cu–Al LDH materials.

This work illustrates, for the first time, the use of Cu–Al LDH intercalated urea-derived anions for the direct production of formaldehyde with high selectivity (>99%) from the GHGs. No sacrificial scavenger material was used in this work. The reaction was performed under visible light, at room temperature, and under atmospheric pressure. The highest activity was for material prepared at U/M = 10, MW = 270 wt, and $M^{II}/M^{III} = 3$: 1. Under the reaction conditions, the converted amounts were 7.48 and 1.02 mmol mL^{-1} g^{-1} for CH_4 and CO_2, respectively. The presence of excess water enhances the stability and durability of the LDH catalysts over several reaction cycles. Increasing the LDH catalyst dosage resulted in a decrease in conversion percent and formaldehyde selectivity. Thus, this work provides a green chemistry approach to utilizing visible light energy, GHGs, and low-cost environmentally friendly photocatalysts to produce valuable products.

Ethics approval and consent to participate

The authors have approved and participated in the manuscript.

Consent for publication

Publication has been approved by the authors.

Data availability

All related data and materials are within the manuscript.

Author contributions

Ayat A.-E. Sakr: conceptualization, methodology, validation, investigation, resources, writing – original draft, writing – review & editing, visualization, project administration, funding acquisition, supervision. Dalia R. Abd El-Hafiz: methodology, validation, investigation, resources, supervision, project administration. Osama Elgabry: methodology, Eman S. Abdulla: methodology. Mohamed A. Ebiad: methodology, validation. Tamer Zaki: supervision.

Conflicts of interest

The authors declare no competing interests.

Acknowledgements

The authors wish to thank Science, Technology & Innovation Funding Authority (STDF) (Project ID: STDF 33496) for their financial support of this work. Also, the authors would like to greatly thank the teams of EPRI Central Labs for their support during this research.

References

1 S. Sonwani and P. Saxena, *Greenhouse Gases: Sources, Sinks and Mitigation*, Springer Nature Singapore Pte Ltd, 2022.
2 H.-O. Pörtner, D. C. Roberts, E. S. Poloczanska, K. Mintenbeck, M. Tignor, A. Alegría, M. Craig, S. Langsdorf, S. Löschke, V. Möller and A. Okem, in *Climate Change 2022: Impacts, Adaptation and Vulnerability. Contribution of Working Group II to the Sixth Assessment Report of the Intergovernmental Panel on Climate Change*, ed. H.-O. Pörtner, D. C. Roberts, M. Tignor, E. S. Poloczanska, K. Mintenbeck, A. Alegría, M. Craig, S. Langsdorf, S. Löschke, V. Möller, A. Okem and B. Rama, Cambridge University Press, Cambridge, UK, 2022.
3 UNFCCC, in *CONFERENCE OF THE PARTIES. Third session Kyoto, 1-10 December 1997 Agenda item 5, United Nations Framework Convention on Climate Change*, 1997, pp. 1–24.

4 G. Myhre, D. Shindell, F.-M. Bréon, W. Collins, J. Fuglestvedt, J. Huang, D. Koch, J.-F. Lamarque, D. Lee, B. Mendoza, T. Nakajima, A. Robock, G. Stephens, T. Takemura and H. Zhang, in *Climate Change 2013: The Physical Science Basis. Contribution of Working Group I to the Fifth Assessment Report of the Intergovernmental Panel on Climate Change*, ed. T. F. Stocker, D. Qin, G.-K. Plattner, M. Tignor, S. K. Allen, J. Boschung, A. Nauels, Y. Xia, V. Bex and P. M. Midgley, Cambridge University Press, Cambridge, United Kingdom and New York, NY, USA, 2013.

5 IPCC, *Climate Change 2022: Mitigation of Climate Change. Contribution of Working Group III to the Sixth Assessment Report of the Intergovernmental Panel on Climate Change*, Cambridge University Press, Cambridge, UK and New York, NY, USA, 2022.

6 IEA, *World Energy Outlook 2022*, International Energy Agency (IEA), 2022, **https://www.iea.org/**.

7 BP, *BP Energy Outlook: 2022 edition, BP p.l.c*, 2022.

8 UNEP/CCAC, *Global Methane Assessment: 2030 Baseline Report, Climate and Clean Air Coalition (CCAC) convened by United Nations Environment Programme (UNEP)*, Nairobi, 2022.

9 UNEP/CCAC, *Global Methane Assessment: 2030 Baseline Report. Summary for Policymakers, Climate and Clean Air Coalition (CCAC) convened by United Nations Environment Programme (UNEP)*, Nairobi, 2022.

10 L. Jeffry, M. Y. Ong, S. Nomanbhay, M. Mofijur, M. Mubashir and P. L. Show, *Fuel*, 2021, **301**, 121017.

11 S. Zhao, H. Liang, X. Hu, S. Li and K. Daasbjerg, *Angew. Chem., Int. Ed.*, 2022, **61**, e202204008.

12 Q. Li, Y. Ouyang, H. Li, L. Wang and J. Zeng, *Angew. Chem., Int. Ed.*, 2022, **61**, e202108069.

13 M. Aresta, *Carbon Dioxide as a Direct Chemical Feedstock*, WILEY-VCH Verlag GmbH & Co. KGaA, Weinheim, 2010.

14 D. M. D'Alessandro, B. Smit and J. R. Long, *Angew. Chem., Int. Ed.*, 2010, **49**, 6058–6082.

15 C. Y. Toe, C. Tsounis, J. Zhang, H. Masood, D. Gunawan, J. Scott and R. Amal, *Energy Environ. Sci.*, 2021, **14**, 1140–1175.

16 Y. H. Park, G. Murali, J. K. R. Modigunta, I. In and S. Il In, *Front. Chem.*, 2021, **9**, 1–7.

17 S. Petit and J. Madejova, *Handbook of Clay Science*, 2013, vol. 5.

18 D. G. Evans and R. C. T. Slade, in *Structure and Bonding*, ed. D. M. P. Mingos, Springer-Verag Berlin Heidelberg, Germany, 2006, vol. 119, pp. 1–87.

19 F. Cavani, F. Trifiro and A. Vaccari, *Catal. Today*, 1991, **11**, 173–301.

20 J. He, M. Wei, B. Li, Y. Kang, D. G. Evans and X. Duan, in *Struct. Bond.*, ed. D. M. P. Mingos, © Springer-Verlag Berlin Heidelberg, 2006, vol. 119, pp. 89–119.

21 X. Long, Z. Wang, S. Xiao, Y. An and S. Yang, *Biochem. Pharmacol.*, 2016, **19**, 213–226.

22 M. P. Jerome, F. A. Alahmad, M. T. Salem and M. Tahir, *J. Environ. Chem. Eng.*, 2022, **10**, 108151.

23 D. Yan, J. Lu, M. Wei, D. G. Evans and X. Duan, *J. Mater. Chem.*, 2011, **21**, 13128–13139.

24 G. Zhang, X. Zhang, Y. Meng, G. Pan, Z. Ni and S. Xia, *Chem. Eng. J.*, 2020, **392**, 123684.

25 J. Wang, R. Li, D. Zeng, W. Wang, Y. Zhang, L. Zhang and W. Wang, *Chem. Eng. J.*, 2023, **452**, 139505.

26 N. Dewangan, W. M. Hui, S. Jayaprakash, A. Bawah, A. J. Poerjoto, T. Jie, A. Jangam, K. Hidajat and S. Kawi, *Catal. Today*, 2020, **356**, 490–513.

27 J. Li, S. Zhang, Y. Chen, T. Liu, C. Liu, X. Zhang, M. Yi, Z. Chu and X. Han, *RSC Adv.*, 2017, **7**, 29051–29057.

28 I. Bilecka and M. Niederberger, *Nanoscale*, 2010, **2**, 1358–1374.

29 P. Benito, F. M. Labajos and V. Rives, *Pure Appl. Chem.*, 2009, **81**, 1459–1471.

30 M. Baghbanzadeh, L. Carbone, P. D. Cozzoli and C. O. Kappe, *Angew. Chem., Int. Ed.*, 2011, **50**, 11312–11359.

31 S. Faramawy, T. Zaki, A. A. E. Sakr, O. Saber, A. K. Aboul-Gheit and S. A. Hassan, *J. Nat. Gas Sci. Eng.*, 2018, **54**, 72–82.

32 A. A.-E. Sakr, T. Zaki, O. Elgabry, M. A. Ebiad, S. M. El-Sabagh and M. M. Emara, *Adv. Powder Technol.*, 2021, **32**, 4096–4109.

33 A. A.-E. Sakr, T. Zaki, O. Elgabry, M. A. Ebiad, S. M. El-Sabagh and M. M. Emara, *Appl. Clay Sci.*, 2018, **160**, 263–269.

34 A. A.-E. Sakr, T. Zaki, O. Saber, S. A. Hassan, A. K. Aboul-Gheit and S. Faramawy, *J. Taiwan Inst. Chem. Eng.*, 2013, **44**, 957–962.

35 R. J. M. J. Vogels, J. T. Kloprogge and J. W. Geus, *J. Colloid Interface Sci.*, 2005, **285**, 86–93.

36 R. Trujillano, M. J. Holgado, F. Pigazo and V. Rives, *Phys. B*, 2006, **373**, 267–273.

37 V. Rives and S. Kannan, *J. Mater. Chem.*, 2000, **10**, 489–495.

38 S. Velu and C. S. Swamy, *Appl. Catal., A*, 1996, **145**, 141–153.

39 K. Jayanthi, P. Vishnu Kamath and G. Periyasamy, *Eur. J. Inorg. Chem.*, 2017, **2017**, 3675–3682.

40 M. R. Berber, I. H. Hafez, K. Minagawa, M. Katoh, T. Mori and M. Tanaka, *J. Mol. Struct.*, 2013, **1033**, 104–112.

41 L. D. S. Neto, C. G. Anchieta, J. L. S. Duarte, L. Meili and J. T. Freire, *ACS Omega*, 2021, **6**, 21819–21829.

42 M. Crivello, C. Pérez, E. Herrero, G. Ghione, S. Casuscelli and E. Rodríguez-Castellón, *Catal. Today*, 2005, **108**, 215–222.

43 X. Li, T. Würger, C. Feiler, R. H. Meißner, M. Serdechnova, C. Blawert and M. L. Zheludkevich, *ACS Omega*, 2022, **7**, 12412–12423.

44 F. Zhao, L. Fan, K. Xu, D. Hua, G. Zhan and S. F. Zhou, *J. CO2 Util.*, 2019, **33**, 222–232.

45 N. Fu, S. Zhang, Y. Ma, Z. Yang and W. Liu, *RSC Adv.*, 2020, **10**, 9808–9813.

46 X. Peng, M. Wang, F. Hu, F. Qiu, T. Zhang, H. Dai and Z. Cao, *J. Environ. Manage.*, 2018, **220**, 173–182.

47 P. Benito, F. M. Labajos, J. Rocha and V. Rives, *Microporous Mesoporous Mater.*, 2006, **94**, 148–158.

48 J. T. Kloprogge, L. Hickey and R. L. Frost, *J. Solid State Chem.*, 2004, **177**, 4047–4057.

49 V. Rives, A. Dubey and S. Kannan, *Phys. Chem. Chem. Phys.*, 2001, **3**, 4826–4836.
50 O. Saber and H. Tagaya, *J. Porous Mater.*, 2003, **10**, 83–91.
51 J. D. Yong, R. Valdez, M. Á. Armenta, N. Arjona, G. Pina-Luis and A. Olivas, *RSC Adv.*, 2022, **12**, 16955–16965.
52 J. M. Hu, Y. Li, Q. Li, Y. F. Zhang, W. Lin and G. X. Jia, *J. Solid State Chem.*, 2004, **177**, 2763–2771.
53 B. Mavis and M. Akinc, *Chem. Mater.*, 2006, **18**, 5317–5325.
54 Y. Qiu and L. Gao, *J. Am. Ceram. Soc.*, 2004, **87**, 352–357.
55 R. Keuleers, G. S. Papaefstathiou, C. P. Raptopoulou, S. P. Perlepes and H. O. Desseyn, *J. Mol. Struct.*, 2000, **525**, 173–183.
56 P. S. Braterman, Z. P. Xu and F. Yarberry, in *Handbook of Layered Materials*, ed. S. M. Auerbach, K. a. Carrado and P. K. Dutta, Marcel Dekker, Inc., 2004.
57 J. T. Kloprogge, L. Hickey and R. L. Frost, *J. Raman Spectrosc.*, 2004, **35**, 967–974.
58 J. J. Lin and T. Y. Juang, *Polymer*, 2004, **45**, 7887–7893.
59 É. Makó, J. Kristóf, E. Horváth and V. Vágvölgyi, *J. Colloid Interface Sci.*, 2009, **330**, 367–373.
60 J. T. Kloprogge, L. Hickey, R. Trujillano, M. J. Holgado, M. S. San Román, V. Rives, W. N. Martens and R. L. Frost, *Cryst. Growth Des.*, 2006, **6**, 1533–1536.
61 R. Keuleers, H. O. Desseyn, B. Rousseau and C. Van Alsenoy, *J. Phys. Chem. A*, 1999, **103**, 4621–4630.
62 J. Grdadolnik and Y. Maréchal, *J. Mol. Struct.*, 2002, **615**, 177–189.
63 R. G. Gavinehroudi, A. Mahjoub, M. Karimi, S. Sadeghi, A. Heydari, H. Mohebali and S. Ghamami, *Green Chem.*, 2022, **24**, 6965–6979.
64 P. R. Jubu, O. S. Obaseki, F. K. Yam, S. M. Stephen, A. A. Avaa, A. A. McAsule, Y. Yusof and D. A. Otor, *J. Opt.*, 2023, **52**(3), 1426–1435.
65 R. Jaiswal, J. Bharambe, N. Patel, A. Dashora, D. C. Kothari and A. Miotello, *Appl. Catal., B*, 2015, **168–169**, 333–341.
66 T. H. Kim, G. Go, H. Cho, Y. Song, C.-G. Lee and Y.-H. Choa, *Front. Chem.*, 2018, **6**, 458.
67 G. D. Gesesse, A. Gomis-berenguer, M. Barthe and C. O. Ania, *J. Photochem. Photobiol., A*, 2020, **398**, 112622.
68 K. Parida, L. Mohapatra and N. Baliarsingh, *J. Phys. Chem. C*, 2012, **116**, 22417–22424.
69 S. Xu, H. Yan and M. Wei, *J. Phys. Chem. C*, 2017, **121**, 2683–2695.
70 S. Nayak and K. M. Parida, *ACS Omega*, 2018, **3**, 7324–7343.
71 N. Ahmed, M. Morikawa and Y. Izumi, *Catal. Today*, 2012, **185**, 263–269.
72 S. Vojkovic, J. Fernandez, S. Elgueta, F. E. Vega, S. D. Rojas, R. A. Wheatley, B. Seifert, S. Wallentowitz and A. L. Cabrera, *SN Appl. Sci.*, 2019, **1**, 1–10.
73 M. Long, P. Hu, H. Wu, Y. Chen, B. Tana and W. Cai, *J. Mater. Chem. A*, 2015, **3**, 5592–5598.
74 M. Lv and H. Liu, *J. Solid State Chem.*, 2015, **227**, 232–238.
75 J. Liqiang, Q. Yichun, W. Baiqi, L. Shudan, J. Baojiang, Y. Libin, F. Wei, F. Honggang and S. Jiazhong, *Sol. Energy Mater. Sol. Cells*, 2006, **90**, 1773–1787.
76 K. Xu, Z. Zhang, G. Chen and J. Shen, *RSC Adv.*, 2014, **4**, 19218–19220.
77 X. X. Guo, T. T. Hua, B. Menga, Y. Sunc and Y.-F. Han, *Appl. Catal., B*, 2020, **260**, 118157.
78 Z. Zhai, X. Yang, L. Xu, C. Hu, L. Zhang, W. Hou and Y. Fan, *Nanoscale*, 2012, **4**, 547–556.
79 L. Mohapatra and K. M. Parida, *Phys. Chem. Chem. Phys.*, 2014, **16**, 20–22.
80 F. Iskandar, A. Fajri, N. Nuraeni, E. Stavila, A. H. Aimon and B. W. Nuryadin, *Mater. Res. Express*, 2018, **5**, 044003.
81 D. Naveena, T. Logu, R. Dhanabal, K. Sethuraman and A. C. Bose, *J. Mater. Sci.: Mater. Electron.*, 2019, **30**, 561–572.
82 R. Gupta, N. K. Eswar, J. M. Modaka and G. Madras, *RSC Adv.*, 2016, **6**, 85675–85687.
83 B. R. Gevers, E. Roduner and F. J. W. J. Labuschagné, *Mater. Adv.*, 2022, **3**, 962–977.
84 M. F. Parveen, S. Umapathy, V. Dhanalakshmi and R. Anbarasan, *J. Mater. Sci.*, 2009, **44**, 5852–5860.
85 J. Li, Z. Mei, L. Liu, H. Liang, A. Azarov, A. Kuznetsov, Y. Liu, A. Ji, Q. Meng and X. Du, *Sci. Rep.*, 2014, **4**, 7240.
86 Y. Cheng, X. Huang, X. Xi and H. Lin, *Ceram. Int.*, 2018, **44**, 5774–5779.
87 Z. Zhang, G. Chen and K. Xu, *Ind. Eng. Chem. Res.*, 2013, **52**, 11045–11049.
88 Y. Jiang, W. Zhao, S. Li, S. Wang, Y. Fan, F. Wang, X. Qiu, Y. Zhu, Y. Zhang, C. Long and Z. Tang, *J. Am. Chem. Soc.*, 2022, **144**, 15977–15987.
89 M. Flores-Flores, E. Luévano-hipólito, L. M. Torres, G. Morales-Mendoza and R. Gómez, *J. Photochem. Photobiol., A*, 2018, **363**, 68–73.
90 S. Wei, X. Zhu, P. Zhang, Y. Fan, Z. Sun, X. Zhao, D. Han and L. Niu, *Appl. Catal., B*, 2021, **283**, 119661.
91 H. Song, X. Meng, S. Wang, W. Zhou, X. Wang, T. Kako and J. Ye, *J. Am. Chem. Soc.*, 2019, **141**, 20507–20515.
92 L. Luo, X. Han, K. Wang, Y. Xu, L. Xiong, J. Ma, Z. Guo and J. Tang, *Nat. Commun.*, 2023, **14**, 2690.
93 Y. Wang, E. Chen and J. Tang, *ACS Catal.*, 2022, **12**, 7300–7316.
94 X. Zhao, H. Jin, Y. Chen and Z. Ge, *Comput. Math. with Appl.*, 2021, **81**, 759–771.
95 B. Tahir, M. Tahir and N. A. S. Amin, *Energy Convers. Manage.*, 2018, **159**, 284–298.
96 B. Tahir, M. Tahir, M. A. C. Yunus, A. R. Mohamed, M. Siraj and A. Fatehmulla, *Appl. Surf. Sci.*, 2020, **520**, 146296.
97 Y. Tokudome, M. Fukui, S. Iguchi, Y. Hasegawa, K. Teramura, T. Tanaka, M. Takemoto, R. Katsura and M. Takahashi, *J. Mater. Chem. A*, 2018, **6**, 9684–9690.
98 J. Chanton, L. Chaser, P. Glasser and D. Siegel, in *Stable Isotopes and Biosphere – Atmosphere Interactions. Processes and Biological Controls*, ed. L. Flanagan, J. Ehleringer and D. Pataki, 2004, pp. 85–105.
99 L. K. Dhandole, S. H. Kim and G. Moon, *J. Mater. Chem. A*, 2022, **10**, 19107–19128.
100 Y. Jiang, S. Li, S. Wang, Y. Zhang, C. Long, J. Xie, X. Fan, W. Zhao, P. Xu, Y. Fan, C. Cui and Z. Tang, *J. Am. Chem. Soc.*, 2023, **145**, 2698–2707.
101 H. Kim, S. Lee, S. Jang, J. haeng Yu, J. S. Yoo and J. Oh, *Appl. Catal., B*, 2021, **292**, 120161.

102 D. Ehhalt, M. Prather, F. Dentener, R. Derwent, E. Dlugokencky, E. Holland, I. Isaksen, J. Katima, V. Kirchhoff, P. Matson, P. Midgley and M. Wang, in *Climate Change 2001: The Scientific Basis, Contribution of Working Group I to the Third Assessment Report of the Intergovernmental Panel on Climate Change (IPPC)*, 2001, pp. 239–287.
103 O. Boucher, P. Friedlingstein, B. Collins and K. P. Shine, *Environ. Res. Lett.*, 2009, **4**, 044007.
104 IPCC, *Climate Change 2013 – The Physical Science Basis*, 2013.
105 S. V. L. Mahlaba, N. H. lal Mahomed, G. M. Leteba, A. Govender and E. van Steen, *ACS Catal.*, 2023, **2023**(13), 14770–14781.
106 Y. Fan, P. Zhang, R. Lu, Y. Jiang, G. Pan, W. Wang, X. Zhu, S. Wei, D. Han and L. Niu, *Catal. Commun.*, 2021, **161**, 106365.
107 T. Kulandaivalu, A. R. Mohamed, K. A. Ali and M. Mohammadi, *Renewable Sustainable Energy Rev.*, 2020, **134**, 110363.
108 Y. Fu, D. Sun, Y. Chen, R. Huang, Z. Ding, X. Fu and Z. Li, *Angew. Chem., Int. Ed.*, 2012, **51**, 3364–3367.
109 Y. Tokudome, T. Morimoto, N. Tarutani, P. D. Vaz, C. D. Nunes, V. Prevot, G. B. G. Stenning and M. Takahashi, *ACS Nano*, 2016, **10**, 5550–5559.
110 A. Kumar and R. Ananthakrishnan, *Green Chem.*, 2020, **22**, 1650–1661.
111 Y. Liao, S.-W. Cao, Y. Yuan, Q. Gu, Z. Zhang and C. Xue, *Chem. – Eur. J.*, 2014, **20**, 10220–10222.
112 N. M. Dimitrijevic, B. K. Vijayan, O. G. Poluektov, T. Rajh, K. A. Gray, H. He and P. Zapol, *J. Am. Chem. Soc.*, 2011, **133**, 3964–3971.
113 A. Ziarati, A. Badiei, R. Grillo and T. Burgi, *ACS Appl. Mater. Interfaces*, 2019, **11**, 5903–5910.
114 K. Katsumata, K. Sakai, K. Ikeda, G. Carja, N. Matsushita and K. Okada, *Mater. Lett.*, 2013, **107**, 138–140.
115 N. Ahmed, Y. Shibata, T. Taniguchi and Y. Izumi, *J. Catal.*, 2011, **279**, 123–135.
116 M. Miyano, H. Zhang, M. Yoshiba and Y. Izumi, *Energy Technol.*, 2017, **5**, 892–900.
117 K. Teramura, S. Iguchi, Y. Mizuno, T. Shishido and T. Tanaka, *Angew. Chem.*, 2012, **124**, 8132–8135.
118 S. Iguchi, K. Teramura, S. Hosokawa and T. Tanaka, *Appl. Catal., A*, 2016, **521**, 160–167.
119 Y. Xu, X. Sun, X. Wang, L. He, M. T. Wharmby, X. Hua, Y. Zhao and Y.-F. Song, *Chem. – Eur. J.*, 2021, **27**, 13211–13220.
120 Q. Guo, Q. Zhang, H. Wang, Z. Liu and Z. Zhao, *Catal. Commun.*, 2016, **77**, 118–122.
121 L. E. Heim, H. Konnerth and M. H. G. Prechtl, *Green Chem.*, 2017, **19**, 2347–2355.
122 B. Niethammer, S. Wodarz, M. Betz, P. Haltenort, D. Oestreich, K. Hackbarth, U. Arnold, T. Otto and J. Sauer, *Chem. Ing. Tech.*, 2018, **90**, 99–112.
123 J. H. Lunsford, *Catal. Today*, 2000, **63**, 165–174.